

Constraining Dark Matter Microphysics with the Annihilation Signal from Subhalos

JACK RUNBURG ¹, ERIC J. BAXTER,² AND JASON KUMAR¹

¹*Department of Physics & Astronomy, University of Hawai'i, Honolulu, HI 96822, USA*

²*Institute for Astronomy, University of Hawai'i, 2680 Woodlawn Drive, Honolulu, HI 96822, USA*

ABSTRACT

In the cold dark matter scenario, galactic dark matter halos are populated with a large number of smaller subhalos. Previous work has shown that dark matter annihilations in subhalos can generate a distinctive, non-Poisson signal in the gamma-ray photon counts probability distribution function (PDF). Here we show that the gamma-ray PDF also carries information about the velocity dependence of the dark matter annihilation cross section. After calculating the PDF assuming *s*-wave and Sommerfeld-enhanced annihilation, we perform a mock data analysis to illustrate how current and future observations can constrain the microphysics of the dark matter annihilation. We find that, with current Fermi data, and assuming a dark matter annihilation cross section roughly at the limit of current bounds from annihilation in dwarf spheroidal galaxies, one can potentially distinguish the non-Poissonian fluctuations expected from dark matter annihilation in subhalos from Poisson sources, as well as from dark matter models with an incorrect velocity-dependence. We explore how robust these results are to assumptions about the modeling of astrophysical backgrounds. We also point out a four-parameter degeneracy between the velocity dependence of the dark matter annihilation, the minimum subhalo mass, the power law index of the subhalo mass function, and the normalization of the dark matter signal. This degeneracy can be broken with priors from N-body simulations or from observational constraints on the subhalo mass function.

1. INTRODUCTION

A key strategy for probing dark matter models is the search for the photons that can be produced when dark matter annihilates in an astrophysical body. Photons are a particularly interesting search channel because they are relatively easy to detect and because they point back to the source (in contrast, charged particles produced in dark matter annihilations will be perturbed by magnetic fields on their passage to Earth). This latter feature has been used to focus on regions of the sky which are known regions of large expected dark matter density, such as the Galactic Center and dwarf spheroidal galaxies (dSphs). Such searches are sensitive to the velocity-dependence of the dark matter annihilation (i.e. its microphysics) in several ways, such as via the angular dependence of the signal [e.g. 1] and via the relative amplitude of the signal from different dSphs [e.g. 2].

Cold dark matter (CDM) models generically predict the existence of a large population of *subhalos* within the main dark matter halo of the Milky Way [3]. The subhalo mass function is expected to rise steeply at small masses, meaning that there are many more small subhalos than large ones. The exact minimum subhalo mass depends on the particle properties of the dark matter, but masses as

low as $1M_{\oplus}$ and below are allowed in several models [e.g. 4]. Unlike dark matter annihilation searches aimed at the Galactic Center or dSphs, the precise positions of small galactic subhalos are unknown if they are not massive enough to host stars. In this paper we consider how the velocity dependence of the dark matter annihilation can be probed by studying the statistics of the unresolved gamma-rays sourced by these subhalos.

The number of photons arriving from any particular direction due to dark matter annihilation in unresolved substructures will generally be drawn from a non-Poissonian distribution [5]. The essential reason is that the photon flux, integrated over a pixel in the sky, will have a non-trivial variance driven by fluctuations in the number of high-luminosity subhalos within the pixel. Although, for a fixed photon flux, the actual photon count is drawn from a Poisson distribution, the convolution of this Poisson distribution with a flux distribution of non-trivial variance is generically non-Poissonian. In particular, a fluctuation in the number of high-luminosity subhalos (that is, a significant fluctuation in the integrated photon flux) could yield a fluctuation in the photon count which would be highly unlikely to arise from a Poisson distribution. An important feature we will find is that different models for the microphysics of dark matter annihilation (in particular, *s*-wave annihilation versus Sommerfeld-enhanced annihilation) produce different non-Poissonian distributions, which can be distinguished from each other with sufficient data. This feature in particular will lend credence to the idea that, with sufficient data, one can not only potentially detect the presence of non-Poissonian fluctuations in the data, but potentially distinguish those which could result from unresolved astrophysical point sources from those which arise from dark matter annihilation (with a variety of microphysical models) in unresolved subhalos.

The non-Poissonian distribution of photon counts depends on the velocity-dependence of the dark matter annihilation cross section because the characteristic dark matter velocity scale depends on the subhalo parameters (such as mass and size) in a manner which is largely determined by dimensional analysis [1]. The subhalo luminosity distribution will thus vary with the choice of dark matter microphysics, since these different choices will differently weight the distribution of subhalo parameters. These differing subhalo luminosity distributions will lead to different non-Poisson photon count distributions, reflecting fluctuations in the photon counts resulting from fluctuations in the number of subhalos along the line of sight.

Our strategy will be to estimate the subhalo parameter distribution using scaling relations obtained from numerical simulations. From this, we will be able to obtain the non-Poissonian photon count distribution arising from *s*-wave and from Sommerfeld-enhanced (in the Coulomb limit) dark matter annihilation.

The photon count distribution has previously been studied for the purpose of determining if *s*-wave dark matter annihilation in unresolved subhalos can be distinguished from astrophysical backgrounds [5, 6]. More recently, the photon counts distribution has been used to investigate whether the GeV photon excess from the Galactic Center (GC) results from the annihilation of a smooth dark matter component, or from a population of unresolved pulsars (see, for example, Lee et al. [7], Bartels et al. [8], Leane and Slatyer [9, 10, 11], Buschmann et al. [12]). The GC analyses in particular point to a message we will echo: distinguishing a signal from background based on the non-Poissonian nature of the distribution observed in data can only be useful if one has some handle on what the signal and background distributions actually are.

We will see that if the background distributions are well-modeled, then an experiment which is able to detect a photon excess above background would also likely be able to determine if this excess is more consistent with s -wave dark matter annihilation, Sommerfeld-enhanced dark matter annihilation, or a Poisson source. But, as with analyses of the GC, we will find that it can be more difficult to distinguish between models for the source distribution if the background is mismodeled. But some discrimination power remains, even in the presence of mismodeled backgrounds, because we are not just looking for non-Poisson fluctuations, but are comparing the likelihoods arising from particular non-Poissonian distributions.

Similarly, we will find that the differences in photon count distributions arising from different dark matter microphysics models can also be replicated by drastic changes to the distribution of subhalo parameters. As background modeling improves, and as the subhalo distributions become more tightly constrained by theory [e.g 13], and data [e.g 14, 15, 16], our results will become more robust.

The plan of this paper is as follows. In §2 we describe the basic formalism for predicting the photon counts distribution from galactic subhalos; in §3 we describe how this formalism can be modified to include the impact of velocity-dependent dark matter annihilation; in §4 we describe our model for gamma-rays produced by astrophysical (i.e. non-dark matter) sources; in §5 we describe the generation and analysis of simulated data. We present our main results in §6 and conclude in §7.

2. THE PHOTON COUNTS DISTRIBUTION FROM SUBHALOS

For simplicity, we will consider an analysis in which we ignore the photon energy information, beyond requiring it to be within the detector acceptance window. We will assume that the sky is divided into pixels, and consider only the number of photons seen by the detector in each pixel over a given exposure.

The basic quantity which we wish to determine is $P_C(C_i)$, the probability of observing C_i counts in the i th pixel over some observation time. To determine this probability distribution function, we follow the analysis of Baxter et al. [6]. We then find

$$P_C(C_i) = \int dF P_{sh}(F; \psi_i) \mathcal{P}[C_i; E_i(F + F_i^{bgd})], \quad (1)$$

where ψ_i is the angle between the i th pixel and the Galactic Center. $P_{sh}(F; \psi_i)$ is the probability distribution for a flux F of photons (with energy within the acceptance of the instrument) to be produced by dark matter annihilation within all subhalos located in the i th pixel. F_i^{bgd} is the flux of photons due to astrophysical foregrounds within the energy range of the instrument, integrated over the solid angle of the i th pixel.¹ E_i is the exposure of the instrument to the i th pixel (i.e. E_i has units of area \times time), and $E_i(F + F_i^{bgd})$ is thus the expected number of photons, from all sources, arriving from the i th pixel. $\mathcal{P}[C_i; E_i(F + F_i^{bgd})]$ is then the Poisson probability for obtaining C_i counts from a Poisson distribution with mean given by $E_i(F + F_i^{bgd})$.

To find $P(C_i)$, we must determine $P_{sh}(F; \psi_i)$. This probability distribution is in turn determined by $P_1(F; \psi_i)$, which is defined as the probability distribution for a single subhalo at angle ψ_i to produce a photon flux F via dark matter annihilation. Essentially, $P_{sh}(F; \psi_i)$ is given by the product of the probability of there being m subhalos within the i th pixel and the probability that those m subhalos

¹ Note, we are ignoring the photon flux arising from dark matter annihilation in the smooth component of the galaxy halo. But at the latitudes on which we will focus, the contribution from the smooth component will be subdominant [17].

produce a total flux F of photons, marginalized over all m . We assume that the probability of there being m subhalos in the i th pixel is Poisson distributed about a mean value $\mu(\psi_i)$. In that case, we may express P_{sh} as [5]

$$P_{sh}(F; \psi_i) = \mathcal{F}^{-1} \{ \exp [\mu(\psi_i) (\mathcal{F}\{P_1(F; \psi_i)\} - 1)] \}, \quad (2)$$

where \mathcal{F} denotes the Fourier transform with respect to F (and \mathcal{F}^{-1} is the inverse Fourier transform), with normalizations defined as in Lee et al. [5]. Given the Poisson statistics of m , the expected standard deviation of the number of subhalos along a line of sight is $\sqrt{\mu}$, so as μ becomes larger, the distribution of m will become narrower around μ . The result is that the flux distribution from all subhalos, $P_{sh}(F)$, will become more δ -function-like as μ increases, leading to a photon count distribution P_C which is more Poisson-like.

$P_1(F; \psi_i)$ is then defined in terms of $P_L(L_{sh}; \ell, \psi_i)$, the probability distribution for a subhalo located at distance ℓ along the line of sight at angle ψ_i from the GC to have intrinsic luminosity L_{sh} . In particular, one finds

$$P_1(F; \psi_i) \propto \theta(F_{\max} - F) \int_0^{\ell_{\max}} d\ell \int dL_{sh} P_L(L_{sh}; \ell, \psi_i) \delta\left(F - \frac{L_{sh}}{4\pi\ell^2}\right), \quad (3)$$

where ℓ_{\max} is the maximum extent of the halo calculated at a given angle ψ_i assuming a halo radius of 220 kpc and $F_{\max} = 10^{-2}$ photons cm^{-2} yr^{-1} . The upper cutoff on the flux arises because it is assumed that halos which produce a flux larger than F_{\max} would be resolved as point sources and not considered part of the unresolved photon flux.

We can proceed further by relating the probability distribution for the subhalo luminosity to the subhalo mass function and the conditional luminosity function, $P_L[L_{sh}|M, r(\ell, \psi_i)]$, which gives the probability for a subhalo of mass M at distance r with respect to the GC to have luminosity L_{sh} . In particular, one finds

$$P_L(L_{sh}; \ell, \psi_i) d\ell \propto \ell^2 d\ell \int_{M_{\min}}^{M_{\max}} dM \frac{d^2 N(r(\ell, \psi_i))}{dM dV} \times P_L[L_{sh}|M, r(\ell, \psi_i)], \quad (4)$$

where $d^2 N/dM dV$ is the subhalo mass function, and M_{\min} and M_{\max} are the minimum and maximum subhalo masses, respectively.

For the subhalo mass function, we adopt a form drawn from numerical simulation:

$$\frac{d^2 N(r)}{dM dV} = A \frac{(M/M_{\odot})^{-\beta}}{\tilde{r}(1 + \tilde{r})^2}, \quad (5)$$

where $\tilde{r} = r/21$ kpc, $A = 1.2 \times 10^4 M_{\odot}^{-1} \text{kpc}^{-3}$, and $\beta = 1.9$ [18]. Here, 21 kpc is roughly the scale radius of the Milky Way, assuming its dark matter distribution is described by a Navarro-Frenk-White (NFW) profile [19]. Note that $P_{sh}(F; \psi_i)$ is largely insensitive to ℓ_{\max} . Although the number of subhalos along the line of sight grows logarithmically with ℓ_{\max} , the photon flux attributable to most distant subhalos scales as ℓ_{\max}^{-2} , implying that the most distant subhalos collectively provide a negligible contribution to P_{sh} .

Our next task is to determine $P_L[L_{sh}|M, r(\ell, \psi_i)]$. Following the approach of Koushiappas et al. [20], we choose

$$P_L[\ln L_{sh}|M, r(\ell, \psi_i)] = \frac{1}{\sqrt{2\pi}\sigma} \exp\left[-\frac{(\ln L_{sh} - \langle \ln L_{sh} \rangle)^2}{2\sigma^2}\right], \quad (6)$$

where $\langle L_{sh} \rangle$ is the mean luminosity for a subhalo of mass M at distance r from the GC, and we take $\sigma = 0.74$.²

In Koushiappas et al. [20] the mean subhalo luminosity in galactic-scale halos was estimated from numerical simulation results assuming s -wave annihilation. Adopting model C_0 of Koushiappas et al. [20], which corresponds roughly to Milky Way-like galactic halos, one finds for s -wave annihilation

$$\langle \ln(L_{sh}/s^{-1}) \rangle = 77.4 + 0.87 \ln(M/10^5 M_\odot) - 0.23 \ln(r/50 \text{kpc}) + \ln \left(\frac{8\pi\Phi_{PP}}{10^{-28} \text{cm}^3 \text{s}^{-1} \text{GeV}^{-2}} \right), \quad (7)$$

where Φ_{PP} is a normalization parameter which is determined by the dark matter microphysics, as we will see in the next section.

We will now generalize the expression for $\langle \ln L_{sh} \rangle$ to the scenario in which dark matter annihilation has a non-trivial velocity-dependence. To do so, we must consider the generic dependence of the subhalo luminosity on the subhalo parameters.

3. INCORPORATING THE IMPACT OF VELOCITY-DEPENDENT ANNIHILATION

We assume that dark matter is a real particle which annihilates with itself with a cross section that can be written as $\sigma v = (\sigma v)_0 \times S(v/c)$, where $(\sigma v)_0$ is independent of the relative velocity v , and $S(v/c) = (v/c)^n$. The standard case of s -wave annihilation thus corresponds to $n = 0$, while p -wave and d -wave annihilation correspond to $n = 2$ and $n = 4$, respectively. Sommerfeld annihilation in the Coulomb limit corresponds to $n = -1$.

The flux of photons arising from dark matter annihilation in a subhalo can be written as

$$\Phi = \Phi_{PP} \times \bar{J}, \quad (8)$$

where

$$\Phi_{PP} = \frac{(\sigma v)_0}{8\pi m_X^2} \bar{N}_\gamma, \quad (9)$$

and \bar{J} is the so-called J -factor, integrated over the full extent of the subhalo. Here, m_X is the mass of the dark matter particle, and \bar{N}_γ is the average number of photons produced per annihilation within the energy range of the observatory. If we assume that the subhalo is at a distance D from the observatory which is much larger than the size of the subhalo, then we may approximate the integrated J -factor as

$$\bar{J} = (1/D^2) \int d^3r \int d^3v_1 \int d^3v_2 f(\vec{r}, \vec{v}_1) f(\vec{r}, \vec{v}_2) \times (v/c)^n, \quad (10)$$

where $\vec{v} = \vec{v}_1 - \vec{v}_2$ is the relative velocity, and $f(\vec{r}, \vec{v})$ is the dark matter velocity distribution [21, 22, 23, 24, 25, 26, 27, 28, 1, 29].

One key assumption we will make is that all dark matter subhalos have the same form, and are parameterized by two dimensionful parameters: the scale density ρ_s and the scale radius r_s .³ In this

² There is a mild dependence of the variance on r and the halo mass, but, for simplicity, we ignore this henceforth.

³ In general, subhalos are also characterized by a tidal radius r_t , outside of which dark matter is tidally stripped from the subhalo. We assume that $r_t > r_s$. Since, for most halo profiles, dark matter annihilation is highly suppressed outside of the scale radius, the J -factor has negligible dependence on r_t .

case, the dependence of \bar{J} on the halo parameters is determined entirely by dimensional analysis. Since the only velocity scale in the problem is $(4\pi G_N \rho_s r_s^2)^{1/2}$, the integrated J -factor may be written as [1]

$$\bar{J} \propto \frac{\rho_s^2 r_s^3}{D^2} (4\pi G_N \rho_s r_s^2)^{n/2}, \quad (11)$$

where the dimensionless proportionality constant is determined only by n and the form of the dark matter distribution, but is independent of the parameters ρ_s and r_s .

Rather than deal with the parameter ρ_s , it will be convenient to define a scale mass parameter, $M_s \equiv \rho_s r_s^3$. For an NFW profile, the halo mass is proportional to M_s up to a logarithmic dependence on the tidal radius. We then see that the photon luminosity of any subhalo can be expressed as

$$L_n \propto \frac{M_s^2}{r_s^3} (4\pi G_N M_s / r_s)^{n/2}, \quad (12)$$

up to a constant which depends on the functional form of the profile but not on the parameters.

We are still left with two halo parameters, M_s and r_s . However, a variety of simulation and semi-analytic results have led to a scaling relation which relates r_s to the halo mass and the distance r from the GC [20]. In particular, the mean luminosity relationship found in Eq. 7,

$$\langle L_{sh}(n=0) \rangle \propto M^{0.87} r^{-0.23}, \quad (13)$$

implies (assuming $M \propto M_s$) the scaling relation

$$r_s \propto M_s^{0.38} r^{0.08}, \quad (14)$$

yielding a mean subhalo luminosity which scales as

$$\langle L_{sh}(n) \rangle \propto M^{0.87} r^{-0.23} \times (M^{0.62} r^{-0.08})^{n/2}. \quad (15)$$

We will adopt this relation in our analysis below. Note that the proportionality constant, which we have omitted in Eq. 15, can be simply absorbed into the definition of the normalization parameter, as in Eq. 7.

Above, we have assumed that dark matter subhalos can be described by a two parameter model such as the NFW profile. It is known from N-body simulations, however, that dark matter halos can be triaxial objects [e.g. 30]. Triaxiality could in principle have an effect on the subhalo J -factors. However, we note that subhalo triaxiality is found to decrease at small subhalo mass [31], i.e. the regime most relevant to our analysis. Since our primary intent is to point out the general impact of velocity-dependent dark matter annihilation on the photon statistics from dark matter annihilation in subhalos, we will ignore subhalo triaxiality below.

We now consider how the velocity dependence of the dark matter annihilation impacts the photon counts distribution. We first discuss the high flux tail of $P_1(F)$, as this is what sets the non-Poisson tail of $P_{sh}(F)$ that makes it possible to distinguish between the dark matter subhalo signal and smooth backgrounds. As described in Lee et al. [5], the high- F tail of $P_{sh}(F)$ will follow that of $P_1(F)$ since in the high flux limit, single bright sources are the dominant source of flux. Ignoring the weak dependence of L_{sh} on r , from Eq. 15 we can write $L_{sh} \propto M^\alpha$ with $\alpha = 0.87 + 0.31n$. At large

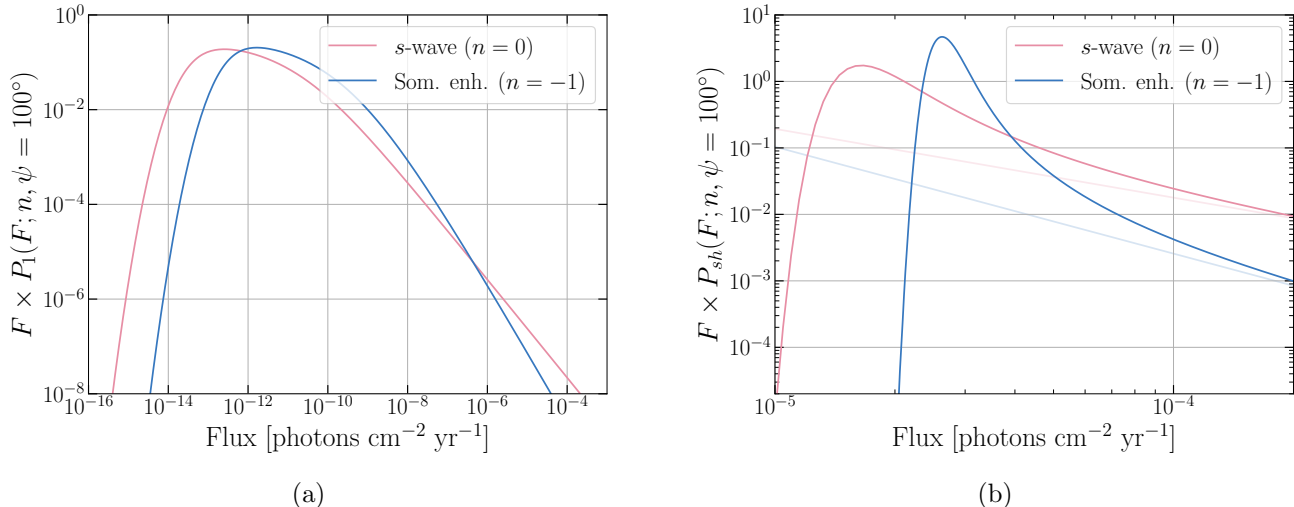


Figure 1. (a) The DM annihilation flux probability distribution for one subhalo $P_1(F; n, \psi_i)$ for s -wave ($n = 0$) and Sommerfeld annihilation ($n = -1$), at $\psi_0 = 100^\circ$. s -wave annihilation results in a flatter power law tail. (b) The DM annihilation flux probability distribution from all subhalos along a line of sight, $P_{sh}(F; n, \psi_i)$. Because Sommerfeld-enhanced annihilation leads to a larger flux contribution from smaller subhalos (which are much more numerous than large subhalos), $P_{sh}(F; n = -1)$ is more tightly peaked than $P_{sh}(F; n = 0)$ (see discussion in §2). The faded lines indicate the expected high flux power law tail expected from Eq. 16.

F , $P_1(F) \propto F^\gamma$, with $\gamma = [(1 - \beta)/\alpha] - 1$ and where β is the power law index of the mass function, as in Eq. 5 [6]. Substituting, we have

$$\gamma \equiv \frac{1 - \beta}{\alpha} - 1 = -\frac{1.03}{1 + 0.36n} - 1. \quad (16)$$

Consequently, larger n (e.g., p -wave or d -wave annihilation) will yield $P_1(F)$ that are flatter than the $P_1(F)$ obtained for small n (Sommerfeld or s -wave). Note that the variance of $P_1(F; n)$ is controlled by F_{\max} for $\gamma > -3$, which encompasses every model that we consider.

Below, we will focus on two scenarios of dark matter annihilation: s -wave annihilation ($n = 0$), and Sommerfeld-enhanced annihilation [32, 33] in the Coulomb limit ($n = -1$). s -wave annihilation is the standard case which is most often considered. Sommerfeld enhancement arises if dark matter particles have an attractive self-interaction mediated by a light particle. The Sommerfeld-enhanced scenario is particularly interesting in the case of annihilation in a subhalo because the relative velocities of particles bound to a subhalo tend to be smaller than the relative velocities of particles bound to the galactic halo. Thus, the signal from Sommerfeld-enhanced dark matter annihilation in a subhalo will be enhanced relative to the signal from the GC. Conversely, p -/ d -wave annihilation will yield signals from subhalos which are suppressed with respect to the GC, so we will not consider them further in this work. But although we focus on s -wave and Sommerfeld-enhanced annihilation, the general arguments that we make below should also apply to e.g. p -wave and d -wave annihilation.

In Figure 1, we plot $P_1(F; n, \psi_i)$ (left panel) and $P_{sh}(F; n, \psi_i)$ (right panel) for $n = 0, -1$, with $\psi_i = 100^\circ$. We take $M_{\min} = 0.1 M_\odot$, $M_{\max} = 10^{10} M_\odot$, yielding $\mu(\psi_i = 100^\circ) = 68539.8$. The normalization of the dark matter signal is chosen to be $\Phi_{PP} = 7 \times 10^{-30} \text{cm}^3 \text{s}^{-1} \text{GeV}^{-2}$ in the case of s -wave annihilation, which roughly corresponds to the upper limit obtained from a search of dwarf

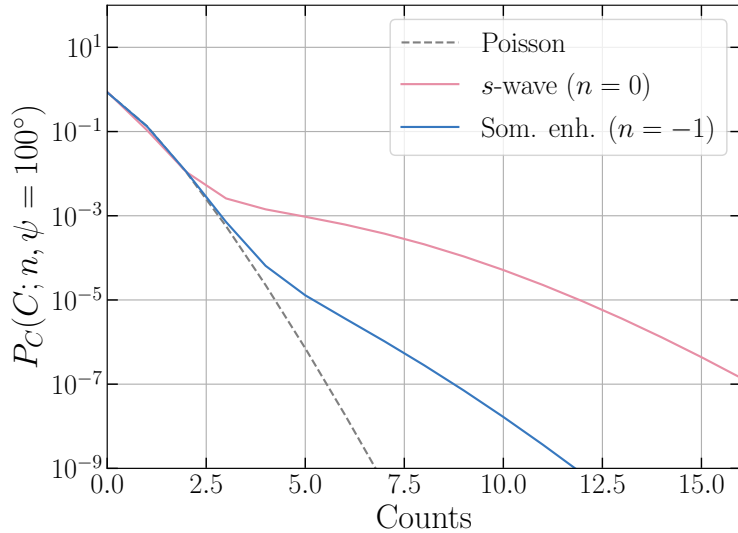


Figure 2. $P_C(C)$ for s -wave and Sommerfeld-enhanced annihilation. The dashed line indicates a Poisson distribution with the mean of $P_{sh}(F; n)$. For both $n = 0, -1$, there is a higher probability to obtain larger counts compared to the Poisson distribution. All count distributions have the same mean.

spheroidal galaxies, as determined by MADHAT [34], assuming a photon energy range of 1-100 GeV. For the case of Sommerfeld enhanced annihilation, we choose the normalization to be such that the expected number of photons from dark matter annihilation is the same as in the s -wave case.

In Fig. 2, we plot $P_C(C; n, \psi_i)$ for $n = 0, -1$ (pink and blue solid lines, respectively), setting $\psi_i = 100^\circ$ and using the same parameter values as above. To compute the photon counts distribution we must assume an exposure (see e.g. Eq. 1). We assume Fermi-like observations with a collecting area of 2000 cm^2 , a field of view of seven steradians, and an observations time of five years, yielding an exposure of $5570.5 \text{ cm}^2 \text{ yr}$. We use a pixel size of 0.21 deg^2 , corresponding to a `healpix` map with $N_{\text{side}} = 128$. We also plot a Poisson distribution (dashed, gray line) with mean identical to that of the $P_C(C; n)$ curves. Note that $P_C(C; n = -1)$ is much closer to a Poisson distribution than $P_C(C; n = 0)$. The reason is because $P_{sh}(F; n = -1)$ has a high- F tail which falls off more steeply than $P_{sh}(F; n = 0)$ (see eq. 16 and Fig. 1), implying that P_{sh} has a smaller variance for the Sommerfeld-enhanced case. As $P_{sh}(F)$ begins to look more like a δ -function, $P_C(C)$ begins to look more like a Poisson distribution.

4. BACKGROUND MODEL

To perform a realistic mock data analysis, we must include the impact of astrophysical gamma-ray backgrounds. Our estimate of astrophysical backgrounds is derived from the models developed by [35]. These models include a diffuse galactic component (`gll_iem_v07.fits`) and an isotropic component (`iso_P8R3_SOURCE_V2_FRONT_v1.txt`). For simplicity, we use the front-converting events in the energy range $1 \text{ GeV} - 3 \text{ TeV}$ because the acceptance is roughly constant for these events. The diffuse galactic gamma-ray background originates primarily from the interaction of cosmic rays with the galactic matter and radiation fields. The Fermi-LAT collaboration [35] construct a set of templates to fit galactic gamma-ray emission sources, and fit these to Fermi Large Area Telescope

data as described in [36]⁴. We refer to the resulting model as the non-isotropic background model. An isotropic background model is also fit to the data as a function of energy. The isotropic component includes unresolved extragalactic contributions, as well as the residual charged particle background.

We introduce the free parameter b_{iso} to scale the normalization of the isotropic background component. In effect, this parameter accounts for some uncertainty in the isotropic background model. For our simulated data, the value of $b_{iso} = 1$ is used and we expect this value to be recovered in our analysis. For simplicity, we keep the normalization of the non-isotropic component fixed. In §6.2, we comment on the effects of mismodelling the galactic background. We note that since the background models are informed by the observed gamma-ray sky, they could potentially already include a dark matter signal. For the purposes of our analysis, however, this is not important as we are merely attempting to provide a rough characterization of the non-dark matter gamma-ray backgrounds.

5. ANALYSIS OF SIMULATED DATA

We now generate and analyze mock data to illustrate how the statistics of the photon count distribution from dark matter annihilations in galactic substructure can be used to constrain the velocity dependence of the annihilation. For simplicity, we assume that all the pixels are statistically independent. In real data, this may not be the case as the instrument beam will correlate nearby pixels. However, we do not expect this simplification to significantly change the conclusions of our analysis. Moreover, the correlation between nearby pixels induced by the beam can always be reduced by increasing the pixel size.

We treat n and Φ_{PP} as the main dark matter parameters of interest, although we will also explore the impact of varying M_{\min} and β in §6.3. Given the choice of these parameters described above, we compute $P_C(C)$ using Eq. 1 for all the pixels of a `healpix` map with $N_{\text{side}} = 128$, corresponding to a pixel size of 0.21 deg^2 . We first consider the signal-only case, for which we set $F_i^{bgd} = 0$. We draw from the resultant distributions to generate realizations of the dark matter signal, as seen in the top row of Fig. 3.

Several features of the signal-only maps are readily apparent. First, the signal increases in amplitude toward the galactic center, as expected from Eq. 7. Second, one can clearly see the non-Poisson nature of the signal. Rather than appearing as a smooth or uniform contribution to the sky, the signal-only maps are dominated by zero-count pixels, with occasional high-count pixels. Finally, it is (somewhat) clear by eye that the s -wave map exhibits more non-Poisson flux than the Sommerfeld enhanced case, as expected from Fig. 2.

Realizations that include backgrounds are generated in the same way, after setting F_i^{bgd} to the flux from the background model discussed in §4. The combined signal and background map are shown in the bottom row of Fig. 3. In each sky map, we mask the region with galactic latitude $|b| < 40^\circ$ since this region will have very large galactic backgrounds. Note that the distinction between the s -wave and Sommerfeld maps that was visible by eye in the signal-only case is no longer visually clear when background is included, requiring a more detailed statistical analysis.

⁴ Updated information on the background modeling can be found at https://fermi.gsfc.nasa.gov/ssc/data/analysis/software/aux/4fgl/Galactic_Diffuse_Emission_Model_for_the_4FGL_Catalog_Analysis.pdf

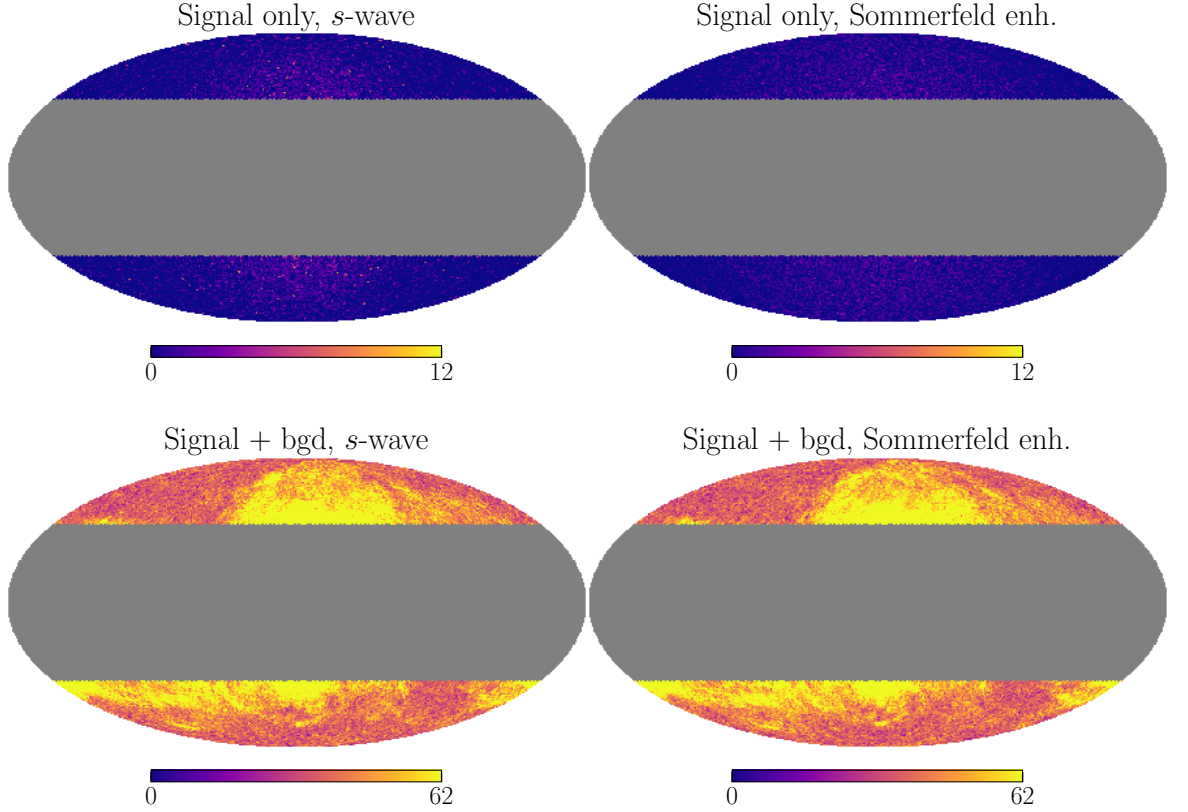


Figure 3. Simulated sky maps in Mollweide projection for s -wave (left) and Sommerfeld-enhanced (right) annihilation, with (top) and without (bottom) astrophysical backgrounds. The Galactic Center is located at the center of the map, and horizontal corresponds to lines of constant galactic latitude. The assumed exposure and dark matter parameters are described in §3, while the background model is described in §4. Consistent with Fig. 2, s -wave annihilation leads to more frequent occurrence of bright pixels. In our analysis, we mask a region within 40° from the galactic plane (grey band) in order to minimize the impact of galactic backgrounds.

The mock data are analyzed as follows. Given our assumption that the pixels are statistically independent, the likelihood for the data can be written as

$$\mathcal{L}(\{C_i\}|\Phi_{PP}, b_{iso}, n) = \prod_{i=1}^N P_C(C_i|\Phi_{PP}, b_{iso}, n, i), \quad (17)$$

where the product runs over all pixels in the map, N . We will also consider an alternate model that removes information from the non-Poisson tail of $P_C(C)$. We have

$$\mathcal{L}^{\text{Poisson}}(\{C_i\}|\Phi_{PP}, b_{iso}, n) = \prod_{i=1}^N \mathcal{P}(C_i|\bar{C}_i(\Phi_{PP}, b_{iso}, n)), \quad (18)$$

where $\mathcal{P}(C_i|\bar{C}_i)$ is the Poisson distribution with mean \bar{C}_i , where

$$\bar{C}_i(\Phi_{PP}, b_{iso}, n) = \sum_{j=0}^{\infty} j P_C(j|\Phi_{PP}, b_{iso}, n, i), \quad (19)$$

is the expected number of photons in the i th pixel. In other words, the Poisson model assumes that the distribution of photon counts is Poissonian with the same mean as the non-Poisson model.

More generally, we can express the expected number of photons per pixel as

$$\langle N_{\text{true}}(n) \rangle = \frac{1}{N} \sum_{i=0}^N \bar{C}_i(\Phi_{PP}, b_{iso}, n). \quad (20)$$

We will find it useful to exchange the parameter Φ_{PP} for $\langle N_{\text{true}}(n) \rangle$. This parameter encodes the normalization of the dark matter annihilation signal (equivalently, the dark matter annihilation cross section), for any choice of n .

One of the goals of this analysis is to determine whether the velocity-dependence of the dark matter annihilation cross section can be determined from the statistics of the photon count distribution. To answer this question, we treat the determination of n from the mock data as a model selection problem. Given two models for the velocity-dependence (specified by values of n), the likelihoods computed from these models can be maximized as a function of the model parameters. Then, the difference in maximum likelihoods for these two models — specified by n and n' — can be computed:

$$\Delta \ln \mathcal{L}_{\text{max}} \equiv \max_{\Phi_{PP}, b_{iso}} [\mathcal{L}(\{C_i\}|\Phi_{PP}, b_{iso}, n)] - \max_{\Phi_{PP}, b_{iso}} [\mathcal{L}(\{C_i\}|\Phi_{PP}, b_{iso}, n')]. \quad (21)$$

Large values of $\Delta \ln \mathcal{L}_{\text{max}}$ (that is, $\gg 1$) would then indicate that the models can be distinguished at high significance from the data; small values, on the other hand, would suggest that there is not sufficient information in the data to distinguish between these possibilities. In this analysis, we will consider two free parameters: the expected number of photons per pixel sourced by dark matter annihilation, $\langle N \rangle$, and the normalization of the isotropic background component, b_{iso} . In an actual data analysis, uncertainty in astrophysical backgrounds is unlikely to be entirely captured by b_{iso} . However, this simple model allows for some uncertainty in the backgrounds, and serves to illustrate several important points. We will consider the impact of additional *systematic* uncertainty in the background model in §6.2.

6. RESULTS

6.1. Ability to distinguish different velocity-dependence models

In Fig. 4 we show constraints on the two parameters of our model — $\langle N \rangle$ and b_{iso} — from the analysis of the mock data. We consider three sets of mock data, in which the data are generated assuming

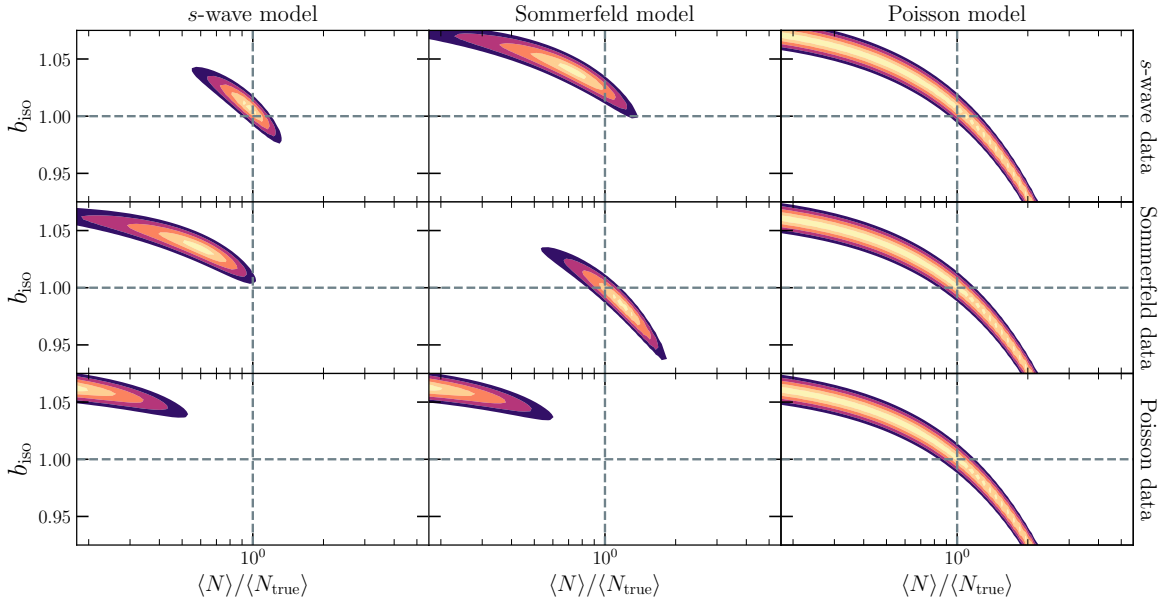


Figure 4. Parameter constraints from the mock data analysis described in §5. The three rows correspond to data generated using three different models: *s*-wave (top), Sommerfeld enhancement (middle), and Poisson (bottom). The contours correspond to 1-, 2-, 3-, 4-, and 5-sigma. In all three cases, we choose the normalization of the dark matter signal to yield the same mean (see §5). The different columns correspond to analyzing the data assuming different models (see labels at top). We vary both the normalization of the dark matter signal, $\langle N \rangle / \langle N_{\text{true}} \rangle$ (i.e. the mean number of photons produced by dark matter annihilation relative to the true mean), and the normalization of the isotropic background, b_{iso} . We see that when the data are analyzed using the correct model, we recover the true parameter values to within the errors (panels along diagonal). We also see some degeneracy between the dark matter signal normalization and the amplitude of the isotropic background. For the Poisson model, this degeneracy is more severe since in this case, the dark matter signal and the isotropic background have the same (Poisson) photon count distribution.

True model	v.s. free b_{iso} + Poisson	v.s. free b_{iso} + <i>s</i> -wave	v.s. free b_{iso} + Sommerfeld
Poisson	—	35.9	19.9
<i>s</i> -wave	21.3	—	35.5
Sommerfeld	24.7	46.3	—

Table 1. The values of $\Delta \ln \mathcal{L}_{\text{max}}$ associated with the indicated model comparisons, computed from mock data. The left column indicates the true model, while the top row indicates the alternate model. Values along the diagonal are 0 by definition. We show values assuming mock data with the current Fermi exposure and with $\langle N_{\text{true}} \rangle = 0.37$. We see that the correct model is preferred with high significance.

either the *s*-wave, Sommerfeld, or Poisson models. For all three cases, the luminosity normalization is chosen so that the average expected number of photons per pixel is fixed to $\langle N_{\text{true}} \rangle = 0.37$, which corresponds to a Φ_{PP} normalization roughly at the limit of Fermi searches for gamma rays from dark matter annihilation in dSphs.

Note that $\bar{C}(\psi_i; n) = E_{i\mu}(\psi_i) \int dF F \times P_1(F; \psi_i; n)$, where the dependence of \bar{C} on n essentially factorizes from its dependence on ψ_i , because the dependence on n arises only from the luminosity distribution $P_L(\ln L_{sh})$, which is nearly independent of ψ_i . Thus, normalizing the s -wave and Sommerfeld models such that they produce the same number of photons averaged over all pixels means that the expected photon counts in each pixel will also be the same for the two models, i.e. $\bar{C}(\psi_i; n = 0) = \bar{C}(\psi_i; n = -1)$ for every pixel i . However, even if the expected photon counts for two models are matched, the photon count *distributions* for each pixel will not be the same in the two models. This scenario is therefore very different from studies of the velocity-dependence of dark matter annihilation in dSphs [2]. In that case, since one is observing resolved dark matter subhalos with particular halo parameters, a change in the velocity dependence of dark matter annihilation can lead to changes in the expected photon counts from various dSphs which cannot be compensated by an overall normalization change. Information about the velocity dependence of the dark matter annihilation is therefore contained in the relative fluxes from dSphs. In the present case, differences in the expected photon counts for two models can be compensated by an overall normalization change, so information about the velocity dependence of the dark matter annihilation must be extracted from the (non-Poisson) photon count distribution in each pixel.

We see from Fig. 4 that when the data are analyzed with the correct model (i.e. the panels along the diagonal), the input parameters are recovered to within the errorbars. The precision of the constraints is also encouraging: even with current Fermi data, there appears to be sufficient statistical power in the data to constrain the dark matter signal normalization to high precision. This is consistent with the findings of [6].

We see that there is significant anti-correlation between the signal amplitude and the isotropic background normalization parameter, b_{iso} . This is not too surprising: more signal photons can be partially compensated by a reduced isotropic background. In the case of Poisson model analysis, this degeneracy is extreme because both the isotropic background model and the Poisson dark matter model are described by Poisson distributions.⁵ The fact that this degeneracy is less severe when the data are analyzed with the s -wave and Sommerfeld models suggests that the non-Poisson information in these models is contributing significantly to the constraints.

When the data are analyzed with the incorrect dark matter model (off-diagonal panels of Fig. 4), the recovered parameters constraints are generally biased. The fact that this bias is small when the data are analyzed with the Poisson model likely reflects the fact that this model effectively discards non-Poisson information. With only the Poisson information, all that matters is the total photon counts, and these will only be recovered when $\langle N \rangle = \langle N_{\text{true}} \rangle$. The bias becomes severe in the non-Poisson cases.

In Table 1 we present the $\Delta \ln \mathcal{L}_{\text{max}}$ values for the model comparisons computed with the mock data. Values of $\Delta \mathcal{L}_{\text{max}} \gg 1$ indicate that in each case, even the current Fermi exposure is sufficient to distinguish the true velocity-dependence model from an incorrect model at high significance. As expected, it is most difficult to distinguish between Sommerfeld-enhanced annihilation and a Poisson-distributed photon source, because the photon count distribution arising from Sommerfeld-enhanced annihilation in subhalos looks close to Poisson.

⁵ Note that the degeneracy must be broken at some level, since the Poisson dark matter model decreases in amplitude away from the Galactic Center, while the isotropic background is uniform across the sky.

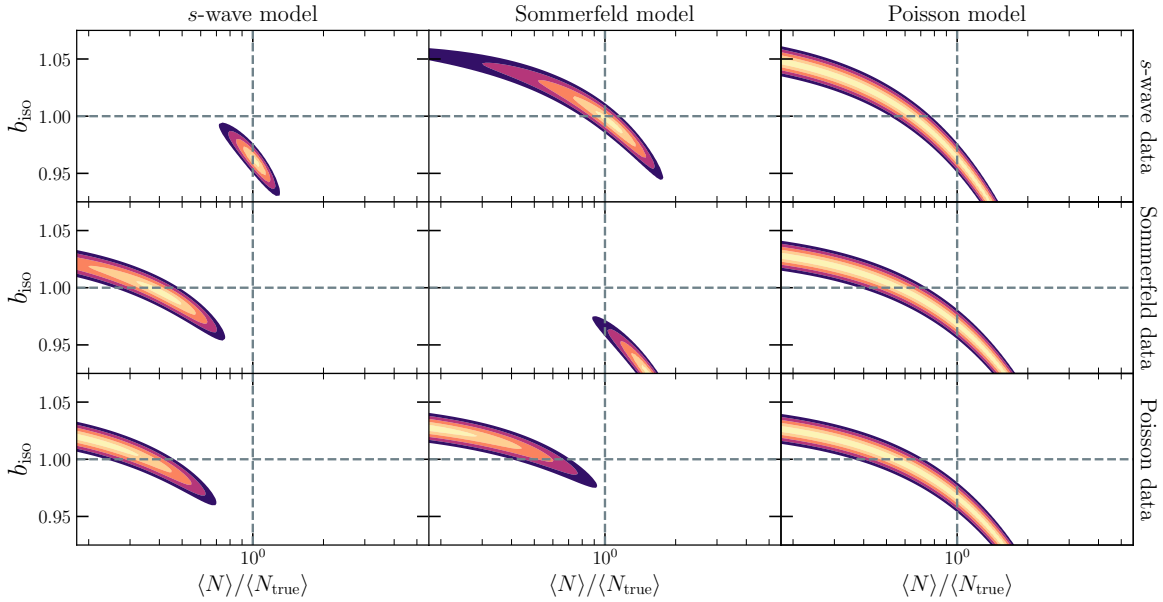


Figure 5. Same as Fig. 4, except the model for the non-isotropic galactic backgrounds used to compute likelihoods has a normalization that is 3% larger than the normalization of the mock data (see §6.2). In this case, we do not recover the input parameters, even when the dark matter model is correct.

True model	v.s. free $b_{\text{iso}} + \text{Poisson}$	v.s. free $b_{\text{iso}} + s\text{-wave}$	v.s. free $b_{\text{iso}} + \text{Sommerfeld}$
Poisson	—	35.3	19.2
$s\text{-wave}$	43.5	—	55.3
Sommerfeld	49.9	67.4	—

Table 2. The values of $\Delta \ln \mathcal{L}_{\text{max}}$ associated with the indicated model comparisons, where the model has a mismodelled galactic background at 103% of the ‘true’ value. The left column indicates the true model, while the top row indicates the alternate model. Values along the diagonal are 0 by definition. We show values assuming mock data with the current Fermi exposure and with $\langle N_{\text{true}} \rangle = 0.37$. We see that the correct model is preferred with high significance.

6.2. Sensitivity to background modeling assumptions

Thus far, we have assumed that uncertainty in our model of astrophysical backgrounds is fully encapsulated in the scaling of the isotropic background component through the parameter b_{iso} . Of course, this is unlikely to be the case in any real data analysis, given the complexity of the galactic gamma-ray backgrounds. We now consider two specific examples in which the non-isotropic backgrounds are mismodelled. In the both examples, we consider the mock data generated as described in §6.1, using the background model described in §4. But in the first case, likelihoods are evaluated assuming that the amplitude of the anisotropic background is 3% larger than that of the true background model. In the second case, likelihoods are evaluated assuming that the amplitude of the anisotropic background is 3% smaller. These simple examples are meant to explore our sensitivity to possible systematic errors in the modeling of the gamma-ray backgrounds.

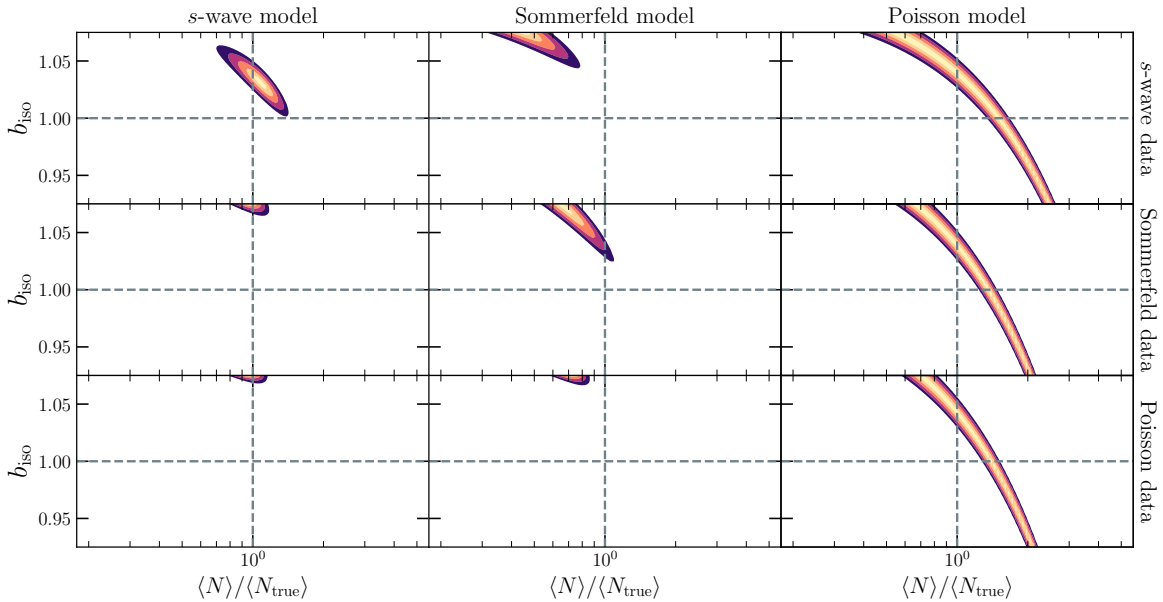


Figure 6. Same as Fig. 5, but for the case when the model for the non-isotropic galactic backgrounds is 3% smaller than the normalization of the mock data (see §6.2). As in Figure 5, we do not recover the input parameters, even when the dark matter model is correct.

In the case where the anisotropic background model overestimates the true anisotropic background, the resultant parameter constraints are shown in Fig. 5. In Table 2 we present the associated $\Delta \ln \mathcal{L}_{\max}$ values. We find that if mock data is generated with *s*-wave annihilation, then an analysis assuming *s*-wave annihilation can recover the correct normalization of the dark matter signal even when the anisotropic background is mismodeled. In this case, the effect of the overestimated anisotropic background is to suppress the recovered normalization of the isotropic background. On the other hand, if mock data is generated with Sommerfeld-enhanced annihilation, an analysis assuming Sommerfeld-enhanced annihilation and a mismodeled anisotropic background would recover a dark matter signal which is too large, and an isotropic background whose normalization is too small.⁶

But, perhaps unexpectedly, we find that, even if the anisotropic background is overestimated, it is still possible to distinguish the correct velocity-dependence of dark matter annihilation. In particular, if the mock data are generated assuming a Poisson-distributed signal, then that model will be preferred over either *s*-wave or Sommerfeld-enhanced annihilation, even with a mismodeled background. This may seem counterintuitive, and contrary to some of the lessons learned from studies of the GC excess, because a Poisson fluctuation about the true mean may appear to be a non-Poissonian fluctuation about a mismodeled mean. In this case, model discrimination is possible because we are not looking for non-Poisson fluctuations, but rather are comparing the data to a particular non-Poisson distribution.

⁶ Note, though, that if mock data is generated assuming *s*-wave dark matter annihilation, but analyzed assuming Sommerfeld-enhanced annihilation, the correct normalization of the dark matter signal is recovered. This appears to be a coincidence.

True model	v.s. free b_{iso} + Poisson	v.s. free b_{iso} + s -wave	v.s. free b_{iso} + Sommerfeld
Poisson	—	36.1	20.1
s -wave	1.3	—	17.6
Sommerfeld	5.2	29.9	—

Table 3. The values of $\Delta \ln \mathcal{L}_{\text{max}}$ associated with the indicated model comparisons, fit with a model with a mismodelled galactic background at 97% of the value used to generate the data. The left column indicates the true model, while the top row indicates the alternate model. Values along the diagonal are 0 by definition. We show values assuming mock data with the current Fermi exposure and with $\langle N_{\text{true}} \rangle = 0.37$. We see that the correct model is again preferred, but with lower significance than in the case of an overestimated background.

Model	underestimated	overestimated
Poisson	51.6	2.4
s -wave	21.0	30.9
Sommerfeld	35.5	13.5

Table 4. Values of $\Delta \ln \mathcal{L}_{\text{max}}$ when the true model with a correctly modelled background is compared to the same dark matter model, but with the anisotropic background underestimated (first column) or overestimated (second column) by 3%.

For the case in which the anisotropic background model underestimates the true anisotropic background, we plot the parameter constraints in Figure 6, and we list the values of $\Delta \ln \mathcal{L}_{\text{max}}$ in Table 3. These results provide an interesting contrast to the case in which the background is overestimated. In either case, one is able to distinguish the true model for the dark matter signal from an incorrect non-Poisson model, though the significance is weaker when the background model underestimates the true background. But if the background model underestimates the true background, then it is difficult to reject a Poisson model for the dark matter signal; even if the true model is non-Poisson, the Poisson model will be only slightly disfavored. The reason is because, if the anisotropic background model underestimates the true anisotropic background, then there is a significant excess of photons, beyond that predicted by the background model, which is Poisson-distributed but anisotropic. This excess is in addition to any photons arising from dark matter annihilation. Although the best fit arises from increasing the amplitude of the Poisson-distributed isotropic background and adding a source with the correct non-Poissonian distribution, the log likelihood is only slightly smaller if one adds a Poisson-distributed source of photons with the same spatial distribution as the dark matter signal.

In Table 4, we compare the maximum likelihood obtained for each true model of dark matter annihilation, when analyzed with the correct dark matter model and correct background model, as compared to the correct dark matter model but incorrect background model, with the anisotropic background either underestimated or overestimated by 3%. As expected, we find a preference for the model with the correct anisotropic background normalization. But interestingly, in the case where the dark matter signal photons are Poisson-distributed, the model with a correctly-modelled anisotropic background is only slightly preferred to the model in which the anisotropic background is overestimated.

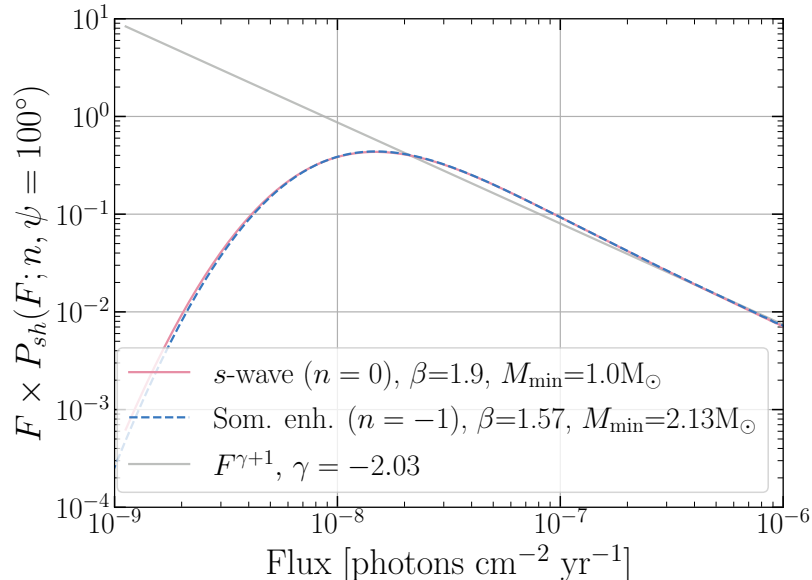


Figure 7. Illustration of the degeneracy between β , M_{\min} , and n discussed in §6.3. We show curves of $P_{\text{sh}}(F; n)$ ($n = -1, 0$ are shown with the blue dashed and red solid lines, respectively). For $n = -1, 0$, we choose $\beta = 1.57, 1.9$, respectively, so as to yield $\gamma = -2.03$ (γ controls the high- F slope of $P_1(F)$ and $P_{\text{sh}}(F)$, as indicated by the solid grey line). For $n = -1, 0$ we choose $M_{\min} = 2.13M_{\odot}, 1.0M_{\odot}$, respectively, so that in both cases we have $\mu(\psi_i = 100^\circ) \approx 51800$. With these choices, we find that $P_{\text{sh}}(F; n = 0)$ and $P_{\text{sh}}(F; n = -1)$ are nearly identical.

6.3. Additional parameter degeneracies

Our analysis above has only varied the dark matter parameters $\langle N \rangle$ and n when fitting the mock data. We now explore parameter degeneracies that can impact our ability to uniquely determine n from measurement of the photon count distribution.

The dark matter signal flux distribution, $P_{\text{sh}}(F)$, is determined by $P_1(F)$ (the flux probability distribution for a single subhalo) and μ (the expected number of subhalos in a pixel) via Eq. 2. The high flux tail of $P_1(F)$ is in turn determined by γ (Eq. 16), which depends on the subhalo mass function (Eq. 5) and luminosity (Eq. 15). It is this high flux tail which sets the non-Poisson tail of the photon counts distribution.

Consider two models for the dark matter annihilation velocity dependence characterized by different values of n . If we adjust model parameters so that γ is the same for these models, then the two models will predict the same power law behavior of $P_{\text{sh}}(F)$ at high F . Obtaining identical values of γ for different values of n can be accomplished by adjusting the β or α values for the two models. If we also adjust parameters (such as M_{\min}) so that μ is the same for both models, then we would expect the resultant $P_{\text{sh}}(F)$ to be very similar, up to an overall normalization. Since we would typically treat the overall flux normalization as a free parameter (since it depends on the unknown properties of the dark matter), it would then be very difficult to distinguish these models from the data.

We explore this possibility in Fig. 7. Here we have adjusted β to keep $\gamma = -2.03$, and have adjusted M_{\min} to keep $\mu(\psi_i = 100^\circ) \approx 51800$. For the curves with $n = -1$ and $n = 0$, we use $\beta = 1.57$ and $\beta = 1.9$ with $M_{\min} = 2.13 M_{\odot}$ and $M_{\min} 1.0 M_{\odot}$, respectively, while maintaining $M_{\max} = 10^{10} M_{\odot}$ in both cases. Once these adjustment are made, we scale the luminosity normalization to match the

mean flux of the two distributions. The agreement between the three curves in Fig. 7 confirms the expected degeneracy between M_{\min} , β , n , and the subhalo luminosity normalization (equivalently, the normalization of the dark matter annihilation cross section). We note that while Fig. 7 varies β as an example, a similar result would be achieved by varying α , as both parameters impact γ . Moreover, similar degeneracies could result if additional freedom were introduced into the subhalo mass function and mass-luminosity relation. In general, since changing n changes the high-flux tail of $P_1(F)$, any variation of parameters that also modifies the high flux tail of $P_1(F)$ while preserving μ could result in a degeneracy that interferes with our ability to measure n .

The impact of these parameter degeneracies on our ability to determine the velocity dependence of the dark matter annihilation can be ameliorated with prior information on the mass function or mass-luminosity relation. Changing n results in a significant change to $P_{sh}(F)$, and counteracting these changes requires fairly extreme variations in other parameters. For example, we needed to change β from 1.9 to 1.57 to produce the overlapping $P_{sh}(F)$ shown in Fig. 7. Consequently, with tight priors on parameters such as β , the impact of the parameter degeneracies highlighted above will be reduced. Prior information on the subhalo mass function and mass luminosity relation can be obtained, for instance, from high resolution N -body simulations [e.g. 37]. Observational constraints from, for instance, strong gravitational lensing [14, 15, 16], can also provide prior information on the subhalo mass function.

7. CONCLUSION

We have shown that the statistics of photons produced in dark matter annihilation in galactic subhalos carries information about the velocity dependence of the annihilation of the dark matter. As seen in, e.g., Fig. 1, s -wave annihilation ($n = 0$) in subhalos leads to a flatter tail in the probability distribution for the flux along a given line of sight than Sommerfeld enhanced annihilation ($n = -1$). For larger n models — e.g., p -wave ($n = 2$) and d -wave ($n = 4$) annihilation — the tail will be even more pronounced. As a result, models with large n will result in very non-Poisson photon count distributions. The fundamental reason for this can be seen in Eq. 15: larger n causes the subhalo luminosity to increase faster with subhalo mass, leading to a higher probability of each line of sight having a bright subhalo.

Our results suggest that in principle, the photon counts distribution can be used to determine the velocity dependence of dark matter annihilation. Indeed, Table 1 show that there is sufficient statistical power in current data to rule out particular velocity-dependence models.

However, we have also identified several challenges to this program. First, there are degeneracies between the velocity dependence of the annihilation cross section, the subhalo mass function, and the subhalo mass-luminosity relation. These three functions all impact the high flux tail of the subhalo flux probability distribution function. As seen in Fig. 7, with appropriate choices of M_{\min} and Φ_{PP} , a near perfect degeneracy results. Consequently, in order to definitively identify the velocity dependence of the dark matter annihilation, we must have robust predictions for the subhalo mass function and mass-luminosity relation. Such predictions can be obtained from N -body simulations and potentially observations of e.g. gravitational lensing.

A second, perhaps more severe, challenge is that using the photon counts distribution to determine the velocity dependence of the dark matter annihilation will require a precise understanding of astrophysical backgrounds. In contrast to diffuse galactic backgrounds, subhalos generically cause non-Poisson behavior in the photon counts probability distribution function [5, 6]. However, this dif-

ference in the count distributions is not necessarily sufficient to distinguish signal from backgrounds, given the much larger amplitude of the backgrounds. Previous analyses of the GC excess have shown that, even if the photon source is Poisson-distributed, mismodeled backgrounds can be misinterpreted as a non-Poisson-distributed source. But we have shown that, when one compares the likelihoods of a Poisson-distributed source model to a particular non-Poisson-distributed source model, the ability to distinguish the true model is at least somewhat robust against background mismodelling (see Tables 2 and 3).

In particular, even if the true model includes a non-Poissonian photon source, it seems possible to robustly reject a model with a different non-Poisson distribution. On the other hand, if the background model leaves a Poisson-distributed background photon source unaccounted for, then it may be difficult to reject a Poisson model for the photons arising from dark matter annihilation, even if the photons sourced by dark matter annihilation are actually non-Poissonian. But note that we performed a relatively simple analysis, assuming only a one-parameter background photon distribution. The only allowed variation in the normalization of the Poisson-distributed background is spatially isotropic. It would be interesting to see if, with a more complete background model, one could better distinguish the presence of a non-Poisson distributed dark matter source from the effects of a mismodelled anisotropic Poisson background.

Furthermore, in this analysis, we have ignored astrophysical backgrounds from unresolved point sources — such as star forming galaxies and blazars — which are likely to also interfere with our ability to identify the dark matter signal. But the fact that we have demonstrated an ability to distinguish between two different non-Poisson-distributed source models, even in the presence of some background mismodelling, gives hope that one can also discriminate the correct model for dark matter annihilation velocity dependence even in the presence of non-Poisson-distributed astrophysical backgrounds.

Finally, we note that our results indicate that, with current Fermi data, one can detect evidence for dark matter annihilation in subhalos with a cross section which is roughly at the sensitivity of dSph searches. This suggests that an application of this technique to the actual Fermi data could be fruitful.

Acknowledgements

JK is supported in part by DOE grant DE-SC0010504. JR is supported by NSF grant AST-1934744.

REFERENCES

- [1] Kimberly K. Boddy, Jason Kumar, Jack Runburg, and Louis E. Strigari. Angular distribution of gamma-ray emission from velocity-dependent dark matter annihilation in subhalos. *Phys. Rev. D*, 100(6):063019, 2019. <https://doi.org/10.1103/PhysRevD.100.063019>.
- [2] Eric J. Baxter, Jason Kumar, Andrew B. Pace, and Jack Runburg. Prospects for measuring dark matter microphysics with observations of dwarf spheroidal galaxies. *Forthcoming*, 3 2021.
- [3] Jurg Diemand, Michael Kuhlen, and Piero Madau. Dark matter substructure and gamma-ray annihilation in the Milky Way halo. *Astrophys. J.*, 657:262–270, 2007. <https://doi.org/10.1086/510736>.
- [4] Anne M. Green, Stefan Hofmann, and Dominik J. Schwarz. The first WIMPy halos. *JCAP*, 2005 (8):003, August 2005. <https://doi.org/10.1088/1475-7516/2005/08/003>.

- [5] Samuel K. Lee, Shin'ichiro Ando, and Marc Kamionkowski. The Gamma-Ray-Flux Probability Distribution Function from Galactic Halo Substructure. *JCAP*, 07:007, 2009. <https://doi.org/10.1088/1475-7516/2009/07/007>.
- [6] Eric J. Baxter, Scott Dodelson, Savvas M. Koushiappas, and Louis E. Strigari. Constraining dark matter in galactic substructure. *PhRvD*, 82(12):123511, December 2010. <https://doi.org/10.1103/PhysRevD.82.123511>.
- [7] Samuel K. Lee, Mariangela Lisanti, Benjamin R. Safdi, Tracy R. Slatyer, and Wei Xue. Evidence for Unresolved γ -Ray Point Sources in the Inner Galaxy. *Phys. Rev. Lett.*, 116(5):051103, 2016. <https://doi.org/10.1103/PhysRevLett.116.051103>.
- [8] Richard Bartels, Suraj Krishnamurthy, and Christoph Weniger. Strong support for the millisecond pulsar origin of the Galactic center GeV excess. *Phys. Rev. Lett.*, 116(5):051102, 2016. <https://doi.org/10.1103/PhysRevLett.116.051102>.
- [9] Rebecca K. Leane and Tracy R. Slatyer. Revival of the Dark Matter Hypothesis for the Galactic Center Gamma-Ray Excess. *Phys. Rev. Lett.*, 123(24):241101, 2019. <https://doi.org/10.1103/PhysRevLett.123.241101>.
- [10] Rebecca K. Leane and Tracy R. Slatyer. Spurious Point Source Signals in the Galactic Center Excess. *Phys. Rev. Lett.*, 125(12):121105, 2020. <https://doi.org/10.1103/PhysRevLett.125.121105>.
- [11] Rebecca K. Leane and Tracy R. Slatyer. The enigmatic Galactic Center excess: Spurious point sources and signal mismodeling. *Phys. Rev. D*, 102(6):063019, 2020. <https://doi.org/10.1103/PhysRevD.102.063019>.
- [12] Malte Buschmann, Nicholas L. Rodd, Benjamin R. Safdi, Laura J. Chang, Siddharth Mishra-Sharma, Mariangela Lisanti, and Oscar Macias. Foreground Mismodeling and the Point Source Explanation of the Fermi Galactic Center Excess. *Phys. Rev. D*, 102(2):023023, 2020. <https://doi.org/10.1103/PhysRevD.102.023023>.
- [13] Piero Madau, Jürg Diemand, and Michael Kuhlen. Dark Matter Subhalos and the Dwarf Satellites of the Milky Way. *ApJ*, 679(2):1260–1271, June 2008. <https://doi.org/10.1086/587545>.
- [14] D. D. Xu, Shude Mao, Jie Wang, V. Springel, Liang Gao, S. D. M. White, Carlos S. Frenk, Adrian Jenkins, Guoliang Li, and Julio F. Navarro. Effects of dark matter substructures on gravitational lensing: results from the Aquarius simulations. *MNRAS*, 398(3):1235–1253, September 2009. <https://doi.org/10.1111/j.1365-2966.2009.15230.x>.
- [15] S. Vegetti, L. V. E. Koopmans, A. Bolton, T. Treu, and R. Gavazzi. Detection of a dark substructure through gravitational imaging. *MNRAS*, 408(4):1969–1981, November 2010. <https://doi.org/10.1111/j.1365-2966.2010.16865.x>.
- [16] Bryan Ostdiek, Ana Diaz Rivero, and Cora Dvorkin. Extracting the Subhalo Mass Function from Strong Lens Images with Image Segmentation. *arXiv e-prints*, art. arXiv:2009.06639, September 2020.
- [17] Volker Springel, Simon D. M. White, Carlos S. Frenk, Julio F. Navarro, Adrian Jenkins, Mark Vogelsberger, Jie Wang, Aaron Ludlow, and Amina Helmi. A blueprint for detecting supersymmetric dark matter in the Galactic halo. *Nature*, 9 2008.
- [18] Volker Springel, Jie Wang, Mark Vogelsberger, Aaron Ludlow, Adrian Jenkins, Amina Helmi, Julio F. Navarro, Carlos S. Frenk, and Simon D. M. White. The Aquarius Project: the subhalos of galactic halos. *Mon. Not. Roy. Astron. Soc.*, 391:1685–1711, 2008. <https://doi.org/10.1111/j.1365-2966.2008.14066.x>.
- [19] Julio F. Navarro, Carlos S. Frenk, and Simon D. M. White. A Universal Density Profile from Hierarchical Clustering. *ApJ*, 490(2):493–508, December 1997. <https://doi.org/10.1086/304888>.
- [20] Savvas M. Koushiappas, Andrew R. Zentner, and Andrey V. Kravtsov. The distribution of annihilation luminosities in dark matter substructure. *Phys. Rev. D*, 82:083504, 2010. <https://doi.org/10.1103/PhysRevD.82.083504>.
- [21] Brant Robertson and Andrew Zentner. Dark Matter Annihilation Rates with Velocity-Dependent Annihilation Cross Sections. *Phys. Rev. D*, 79:083525, 2009. <https://doi.org/10.1103/PhysRevD.79.083525>.

- [22]K. Belotsky, A. Kirillov, and M. Khlopov. Gamma-ray evidences of the dark matter clumps. *Grav. Cosmol.*, 20:47–54, 2014. <https://doi.org/10.1134/S0202289314010022>.
- [23]Francesc Ferrer and Daniel R. Hunter. The impact of the phase-space density on the indirect detection of dark matter. *JCAP*, 09:005, 2013. <https://doi.org/10.1088/1475-7516/2013/09/005>.
- [24]Kimberly K. Boddy, Jason Kumar, Louis E. Strigari, and Mei-Yu Wang. Sommerfeld-Enhanced J -Factors For Dwarf Spheroidal Galaxies. *Phys. Rev. D*, 95(12):123008, 2017. <https://doi.org/10.1103/PhysRevD.95.123008>.
- [25]Yi Zhao, Xiao-Jun Bi, Peng-Fei Yin, and Xinmin Zhang. Constraint on the velocity dependent dark matter annihilation cross section from gamma-ray and kinematic observations of ultrafaint dwarf galaxies. *Phys. Rev. D*, 97(6):063013, 2018. <https://doi.org/10.1103/PhysRevD.97.063013>.
- [26]Mihael Petac, Piero Ullio, and Mauro Valli. On velocity-dependent dark matter annihilations in dwarf satellites. *JCAP*, 12:039, 2018. <https://doi.org/10.1088/1475-7516/2018/12/039>.
- [27]Kimberly K. Boddy, Jason Kumar, and Louis E. Strigari. Effective J -factor of the Galactic Center for velocity-dependent dark matter annihilation. *Phys. Rev. D*, 98(6):063012, 2018. <https://doi.org/10.1103/PhysRevD.98.063012>.
- [28]Thomas Lacroix, Martin Stref, and Julien Laval. Anatomy of Eddington-like inversion methods in the context of dark matter searches. *JCAP*, 09:040, 2018. <https://doi.org/10.1088/1475-7516/2018/09/040>.
- [29]Kimberly K. Boddy, Jason Kumar, Andrew B. Pace, Jack Runburg, and Louis E. Strigari. Effective J -factors for Milky Way dwarf spheroidal galaxies with velocity-dependent annihilation. *PhRvD*, 102(2):023029, July 2020. <https://doi.org/10.1103/PhysRevD.102.023029>.
- [30]Y. P. Jing and Yasushi Suto. Triaxial Modeling of Halo Density Profiles with High-Resolution N-Body Simulations. *ApJ*, 574(2):538–553, August 2002. <https://doi.org/10.1086/341065>.
- [31]Carlos A. Vera-Ciro, Laura V. Sales, Amina Helmi, and Julio F. Navarro. The shape of dark matter subhaloes in the Aquarius simulations. *MNRAS*, 439(3):2863–2872, April 2014. <https://doi.org/10.1093/mnras/stu153>.
- [32]Nima Arkani-Hamed, Douglas P. Finkbeiner, Tracy R. Slatyer, and Neal Weiner. A Theory of Dark Matter. *Phys. Rev. D*, 79:015014, 2009. <https://doi.org/10.1103/PhysRevD.79.015014>.
- [33]Jonathan L. Feng, Manoj Kaplinghat, and Hai-Bo Yu. Sommerfeld Enhancements for Thermal Relic Dark Matter. *Phys. Rev. D*, 82:083525, 2010. <https://doi.org/10.1103/PhysRevD.82.083525>.
- [34]Kimberly K. Boddy, Stephen Hill, Jason Kumar, Pearl Sandick, and Barmak Shams Es Haghi. MADHAT: Model-Agnostic Dark Halo Analysis Tool. *Comput. Phys. Commun.*, 261:107815, 2021. <https://doi.org/10.1016/j.cpc.2020.107815>.
- [35]The Fermi-LAT collaboration. Fermi Large Area Telescope Fourth Source Catalog. *The Astrophysical Journal Supplement Series*, 247(1):33, March 2020. ISSN 1538-4365. <https://doi.org/10.3847/1538-4365/ab6bcb>.

- [36] F. Acero, M. Ackermann, M. Ajello, A. Albert, W. B. Atwood, M. Axelsson, L. Baldini, J. Ballet, G. Barbiellini, D. Bastieri, A. Belfiore, R. Bellazzini, E. Bissaldi, R. D. Blandford, E. D. Bloom, J. R. Bogart, R. Bonino, E. Bottacini, J. Bregeon, R. J. Britto, P. Bruel, R. Buehler, T. H. Burnett, S. Buson, G. A. Caliandro, R. A. Cameron, R. Caputo, M. Caragiulo, P. A. Caraveo, J. M. Casandjian, E. Cavazzuti, E. Charles, R. C. G. Chaves, A. Chekhtman, C. C. Cheung, J. Chiang, G. Chiaro, S. Ciprini, R. Claus, J. Cohen-Tanugi, L. R. Cominsky, J. Conrad, S. Cutini, F. D'Ammando, A. de Angelis, M. DeKlotz, F. de Palma, R. Desiante, S. W. Digel, L. Di Venere, P. S. Drell, R. Dubois, D. Dumora, C. Favuzzi, S. J. Fegan, E. C. Ferrara, J. Finke, A. Franckowiak, Y. Fukazawa, S. Funk, P. Fusco, F. Gargano, D. Gasparrini, B. Giebels, N. Giglietto, P. Giommi, F. Giordano, M. Giroletti, T. Glanzman, G. Godfrey, I. A. Grenier, M.-H. Grondin, J. E. Grove, L. Guillemot, S. Guiriec, D. Hadasch, A. K. Harding, E. Hays, J. W. Hewitt, A. B. Hill, D. Horan, G. Iafate, T. Jogler, G. Jóhannesson, R. P. Johnson, A. S. Johnson, T. J. Johnson, W. N. Johnson, T. Kamae, J. Kataoka, J. Katsuta, M. Kuss, G. La Mura, D. Landriu, S. Larsson, L. Latronico, M. Lemoine-Goumard, J. Li, L. Li, F. Longo, F. Loparco, B. Lott, M. N. Lovellette, P. Lubrano, G. M. Madejski, F. Massaro, M. Mayer, M. N. Mazziotta, J. E. McEnery, P. F. Michelson, N. Mirabal, T. Mizuno, A. A. Moiseev, M. Mongelli, M. E. Monzani, A. Morselli, I. V. Moskalenko, S. Murgia, E. Nuss, M. Ohno, T. Ohsugi, N. Omodei, M. Orienti, E. Orlando, J. F. Ormes, D. Paneque, J. H. Panetta, J. S. Perkins, M. Pesce-Rollins, F. Piron, G. Pivato, T. A. Porter, J. L. Racusin, R. Rando, M. Razzano, S. Razzaque, A. Reimer, O. Reimer, T. Reposeur, L. S. Rochester, R. W. Romani, D. Salvetti, M. Sánchez-Conde, P. M. Saz Parkinson, A. Schulz, E. J. Siskind, D. A. Smith, F. Spada, G. Spandre, P. Spinelli, T. E. Stephens, A. W. Strong, D. J. Suson, H. Takahashi, T. Takahashi, Y. Tanaka, J. G. Thayer, J. B. Thayer, D. J. Thompson, L. Tibaldo, O. Tibolla, D. F. Torres, E. Torresi, G. Tosti, E. Troja, B. Van Klaveren, G. Vianello, B. L. Winer, K. S. Wood, M. Wood, S. Zimmer, and Fermi-LAT Collaboration. Fermi Large Area Telescope Third Source Catalog. *The Astrophysical Journal Supplement Series*, 218:23, June 2015.
- [37] Davide Fiacconi, Piero Madau, Doug Potter, and Joachim Stadel. Cold Dark Matter Substructures in Early-type Galaxy Halos. *ApJ*, 824(2):144, June 2016.
- <https://doi.org/10.3847/0004-637X/824/2/144>.